

## Design methodology of an osculating cone waverider with adjustable sweep and dihedral angles<sup>\*</sup>

Shao-hua CHEN<sup>†</sup>, Jun LIU<sup>†‡</sup>, Wei HUANG, Feng DING

*Science and Technology on Scramjet Laboratory, National University of Defense Technology, Changsha 410073, China*

<sup>†</sup>E-mail: chenshaohua\_nudt@163.com; liujun@nudt.edu.cn

Received Jan. 17, 2020; Revision accepted Apr. 29, 2020; Crosschecked July 15, 2020; Published online Aug. 20, 2020

**Abstract:** When considering the practical engineering application of a waverider, the on-design and off-design aerodynamic characteristics of the design conditions, especially the lift-to-drag ratio and the stability, deserve attention. According to recently studies, the planform and rear sight shape of a waverider are closely related to the above aerodynamic performance. Thus, the planform leading-edge profile curve used to design the planform shape of a vehicle is applied to designing an osculating cone waverider. Two key parameters concerned in planform and rear sight shape, namely the plan view sweep angle of the leading edge and the dihedral angle of the underside are introduced to the waverider design process. Each parameter is inserted in the control curve equation. Especially, a parameterization scheme is put forward for the free adjustment of the sweep angle along the leading edge. Finally, three examples are generated for verification and investigation. After the verification process based on the inviscid flow field of one case, the influences of the sweep and dihedral angles on the lift-to-drag ratio and the lateral static stability are evaluated, and meaningful results are obtained. Based on these results, we can conclude that, considering the maximum lift-to-drag ratio, the sweep angle plays a role on the lift-to-drag ratio only at subsonic and trans/supersonic speed as a negligible effect is observed at hypersonic speeds, whereas the dihedral angle is seem to produce a relevant difference at hypersonic speeds. Considering the lateral static stability, the dihedral angles have more influence on the waverider than the sweep angles.

**Key words:** Osculating cone waverider; Planform leading-edge profile curve; Sweep and dihedral angles; Lift-to-drag ratio; Lateral static stability

<https://doi.org/10.1631/jzus.A2000020>

**CLC number:** V211.1

### 1 Introduction


The waverider (Nonweiler, 1959; Kuchemann, 1978; Ding et al., 2017; Zhang WH et al., 2019) as a promising method for a hypersonic vehicle (Liao et al., 2018; Meng et al., 2019; Wang and Shen, 2019; Wen et al., 2019; Zhang TT et al., 2019) has several advantages, such as a high lift-to-drag ratio at hypersonic speeds (Ding et al., 2015a, 2018). Furthermore, a waverider can be easily parameterized (He et

al., 2009; Rodi, 2011, 2015; Tian et al., 2013; Ding et al., 2015a, 2015b, 2015c) and optimized (Liu et al., 2014; Kontogiannis et al., 2015a, 2017) to improve its aerodynamic characteristics.

The waverider can ride on the shock wave generated by itself. In other words, the shock wave is attached to the leading edge when the waverider is traveling at the design speed. However, there is a premise that the stream surface solved in the inviscid basic flow field is used as the undersurface of a waverider. For design convenience, the quickly solved axisymmetric cone-derived flow field is widely used. Based on the above solution method, a fundamental coned-derived waverider (Jones et al., 1968) was initially put forward and used for hypersonic waverider design. Sobieczky et al. (1990) developed an osculating cone waverider based on a 3D basic flow

<sup>‡</sup> Corresponding author

<sup>\*</sup> Project supported by the National Natural Science Foundation of China (No. 11702322) and the Natural Science Foundation of Hunan Province, China (No. 2018JJ3589)

 ORCID: Shao-hua CHEN, <https://orcid.org/0000-0002-6244-5131>

© Zhejiang University and Springer-Verlag GmbH Germany, part of Springer Nature 2020

field assembled by a spanwise 2D conical flow field. Compared with a cone-derived waverider, the osculating cone waverider has wider design margins when considering the 3D non-axisymmetric basic flow field. The 3D basic flow field used for waverider design can take other forms with varied aerodynamic performances, and not be simply an axisymmetric flow (Ding et al., 2015d; Kontogiannis et al., 2015b). Commonly, the shock wave curve has an infinite radius of curvature along the center part and a finite radius of curvature along the outboard part. Therefore, an osculating cone waverider combines the positive attributes of wedge and conical flow (Liu CZ et al., 2014; Liu Z et al., 2017a, 2017b), and is suitable for the forebody or wing of a hypersonic vehicle. In the practical applications of aircraft in the range from subsonic (Wood and Bauer, 2001) to hypersonic (Rasmussen, 1997; Walker et al., 2008), research shows that aerodynamic performance and control characteristics should not be ignored. Therefore, various aerodynamic characteristics, especially such related geometry parameters as the sweep and dihedral angles, are considered in waverider design in this study.

One key design parameter concerned with lateral stability, the dihedral angle, has been discussed in many open source accounts. Hirschel and Weiland (2009) mentioned a hypersonic vehicle with slight positive (upward) dihedral of the lower side of the vehicle. This dihedral shape improves rolling stability as well as lateral/directional stability. The dihedral effect (Etkin and Reid, 1996) stability condition ( $C_{l\beta} < 0$ ) is put forward to prescribe a limit on the relationship between the dihedral angle and the lateral stability, so that as a consequence of disturbance of the angle of sideslip the airplane will roll away from the disturbance and sideslip will decrease (Pezzella et al., 2014). Computational fluid dynamics (CFD) aerodynamic data show that the dihedral stability of HIFiRE 6 changes with Mach number (Adamczak and Bolender, 2015; Favaloro et al., 2015). Moreover, an unsuccessful flight demonstration of a hypersonic technology vehicle (HTV-2) was due to the uncontrolled vehicle, and was mainly blamed on the lateral stability (Walker et al., 2008). In summary, the aerodynamic shape design of a hypersonic or wide-ranged speed vehicle should consider the dihedral angle as an input parameter.

Strohmeier et al. (1996) and Strohmeier (1998) studied the subsonic/transonic aerodynamic characteristics of two waveriders with different planform shapes. They found that the aerodynamic efficiency, namely the rolling moment coefficient of waverider in subsonic and trans-sonic flow will be improved with a Gothic planform with combined forebody and delta wing planforms. Liu CZ et al. (2017) put forward a waverider design method with a double swept waverider. The research showed that the double swept waverider with the configurations of a vortex-generating edge performed well in subsonic characteristics, aerodynamic stability, and nonlinear vortex lift, while maintaining a high hypersonic lift-to-drag ratio. It can be inferred that the sweep angle ( $\Lambda$ ) shown in Fig. 1 plays an important role in the aerodynamic performance of a waverider similar to the dihedral angle ( $I$ ). Some key planform shape parameters including the sweep angle and the planform area need to be especially adjusted according to the design requirements (Liu et al., 2014, 2016; Viviani and Pezzella, 2015). As shown in Fig. 2, the lower compression surface of a waverider is lofted from a series of shock-affected streamlines that start at the leading edge. The leading edge lies on the shock wave. That is to say, the shock wave attaches to the leading edge when the waverider flies under the designed conditions (Kontogiannis et al., 2015a; Ding et al., 2018). To solve the streamlines, a key step is to find the starting point, namely the leading-edge point at the leading edge. There are different approaches for obtaining this leading edge (Kontogiannis et al., 2015a). Each approach controls a different aspect of the waverider geometry. Traditionally, the upper surface profile curve is adopted as the input geometrical curve to find the leading edge during the waverider design process (Ding et al., 2015d). However, the planform shape lying on the leading-edge planform profile cannot be directly controlled.

He et al. (1993) presented a cone-derived waverider design method. As shown in Fig. 1, the leading edge is the intersection of the horizontal projection of the leading-edge planform profile specified as  $z=f(x)$  and the cone-shaped shock wave corresponding with the dash dotted curve.  $\beta_s$  is the shock angle. Kontogiannis et al. (2015a) collected several waverider design approaches. The planform leading-edge definition (PLED) was used in an osculating

cone waverider design process that is similar to He et al. (1993)'s operation of solving the leading edge. As illustrated in Figs. 2 and 3, the leading-edge point may be located by finding the point intersection between the shock wave trace and the vertical projection of the leading-edge profile curve on the same osculating plane. In Fig. 2,  $Ma_\infty$  is the freestream Mach number. In Fig. 3,  $\alpha_p$  is the inclination angle between osculating plane and vertical plane.

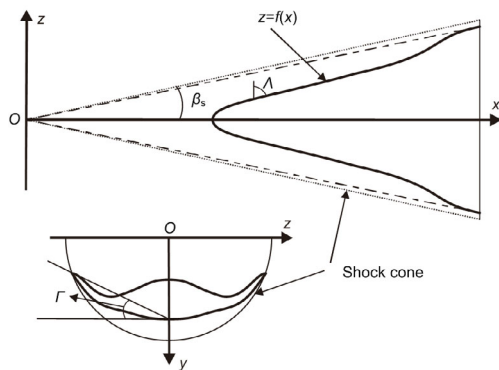


**Fig. 1** Cone-derived waverider design method defined by the leading-edge planform profile

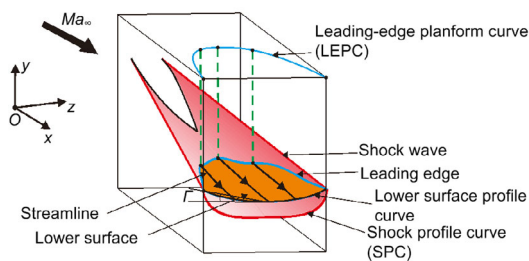


**Fig. 2** Osculating cone waverider design method defined by the leading-edge planform profile

Considering the association of the aerodynamic performance with sweep and dihedral angles, two geometric parameters are introduced to the waverider design procedure in this research. Firstly, this study raises an effective solution for locating the osculating cone waverider leading-edge point. Secondly, to control the sweep and dihedral angles, this study redesigns the leading-edge planform profile curve function and the shock profile curve, taking the above two parameters into consideration. Thirdly, to validate the design methodology in this study, three wa-

veriders with different sweep angle combination schemes or dihedral angles are generated. The aerodynamic performances of these three waveriders are then analyzed. In general, the effects of sweep angle and dihedral angle on the aerodynamic performance, including lift-to-drag ratio and lateral stability, have been evaluated and some notable conclusions are obtained.

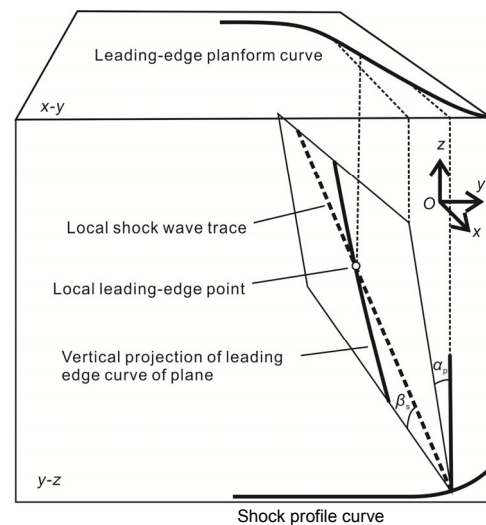


**Fig. 3** Three-dimensional geometrical relations for locating the leading-edge point on each osculating plane for a plan view definition of the leading-edge shape

## 2 Design methodology

### 2.1 Osculating cone waverider design method defined by the planform leading edge

This study uses the osculating cone waverider design method defined by the leading-edge planform profile, as illustrated in Fig. 2. The leading-edge planform curve (LEPC) is used to find the leading edge. As shown in Fig. 2, the 3D leading edge in the shock wave is the vertical projection of the LEPC. There is currently no analytic method that has been developed to solve the intersection between the shock wave and the horizontal projection of the leading-edge planform profile curve. Here, the leading edge is defined by the leading-edge points on several osculating planes. The shock wave determined by the shock wave curve is a smooth surface composed of the shock wave trace on each osculating plane.

As shown in Fig. 4, a streamline starting from the leading-edge point is solved in the osculating plane. The leading-edge point  $P_{le}$  is also the intersection point of the local shock wave trace and the LEPC on each osculating plane. The coordinate of point  $S$  in the shock profile curve is given in the osculating cone waverider method. The coordinate of point  $O$ , known as the cone vertex, depends on the geometrical relationships shown in Fig. 4.  $W$  is the width of waverider, and  $\delta$  is the half cone vertex angle of local osculating cone. The LEPC is defined by the designer. Moreover, the coordinate of the exclusive leading-edge point  $P_{le}(x_{le}, y_{le}, z_{le})$  is restricted by Eq. (1) according to the geometrical relationships between points  $O$  and  $S$  as shown in Fig. 4.

$$\begin{cases} x_{le} \in [x_O, x_S], \\ y_{le} \in [y_O, y_S], \\ z_{le} \in \{\max(\min(z_O, z_S), 0), \min(\max(z_O, z_S), W/2)\}. \end{cases} \quad (1)$$

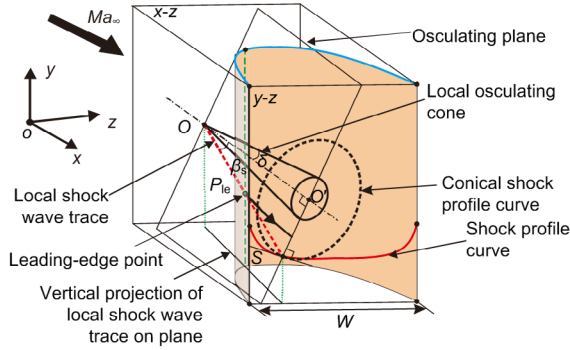


**Fig. 4** Three-dimensional geometrical relationships for locating the leading-edge point on each osculating plane

## 2.2 Design principle

In this study, the osculating cone waverider design methodology with adjustable sweep and dihedral angles is put forward. To control the sweep angle distribution along the leading edge, the LEPC function is defined by the given spanwise distribution of the sweep angle. The dihedral angle is introduced to the shock profile curve function for the purpose of free adjustment. Considering the practicality of the

waverider, the length and width of the waverider are thoroughly restricted when adjusting the sweep and dihedral angles.

### 2.2.1 Adjustable sweep angle

In general, the leading edge of the waverider is divided into several segments with different sweep angle distribution patterns in this study. Thus, the LEPC function is designed as a piecewise equation depicted in Eq. (2).  $A_i(z)$  is the sweep angle distribution function along the  $i$ th segment of the leading edge.  $C$  is the constant of integration. All the distribution functions of all the segments belong to the sweep angle distribution function set  $\kappa$ , and  $n$  is the number of elements in a set of  $\kappa$ . Each subsection of the LEPC function  $f_i(z)$  is solved according to  $A_i(z)$ . The definition of sweep angle  $A$  is illustrated in Fig. 1.

$$\begin{cases} f_i(z) = -\int_{z_i}^z \tan A_i(z) + C, & z \in (z_i, z_{i+1}), \\ z_1 = 0 < \dots < z_i < \dots < z_n = W/2, \\ A_i(z) \in \kappa = \{A(z) | A_1(z), A_2(z), \dots, A_n(z)\}. \end{cases} \quad (2)$$

In order to obtain the analytic expression of  $f_i(z)$ ,  $A_i(z)$  in Eq. (2) is declared to be a constant  $A_i$  within each segment. In Eq. (2), the sweep angle spanwise distribution  $\kappa$  as well as the spanwise coordinate  $z_i$  of each subsection knot are predefined. The leading-edge planform profile curve function is expressed as

$$\begin{cases} f_i(z) = -\tan A_i \cdot (z - z_i) + f_i(z_i), & z \in (z_i, z_{i+1}), \\ z_1 = 0 < \dots < z_i < \dots < z_{n+1} = W/2, \\ A_i \in \kappa = \{A | A_1, A_2, \dots, A_n\}. \end{cases} \quad (3)$$

For practical application, assuming that the length  $L_W$  of the waverider is also regarded as a constraint, which is given by

$$L_W = \sum_{i=1}^n (f_i(z_i) - f_i(z_{i+1})). \quad (4)$$

Through the combination of Eqs. (3) and (4), the constraint equation illustrated in Eq. (5) is obtained:

$$\begin{cases} L = \sum_{i=1}^n (z_{i+1} - z_i) \cdot \tan A_i, \\ z_1 = 0 < \dots < z_i < \dots < z_{n+1} = W/2, \\ A_i \in \kappa = \{A_1, A_2, \dots, A_n\}. \end{cases} \quad (5)$$

Given the input conditions of  $z_i$  and  $\kappa = \{A_1, A_2, \dots, A_n\}$ , Eq. (5) will be an overdetermined function which cannot be solved. For research convenience,  $n=2$  is applied to Eq. (5). Thus, the waverider will have a double-sweep leading edge. The simplification of Eq. (5) is expressed as Eq. (6), in which  $z_2$  is set as the unknown parameter:

$$\begin{cases} L = \Delta W_1 \cdot \tan A_1 + \Delta W_2 \cdot \tan A_2, \\ \Delta W_1 = z_2 - z_1, \\ \Delta W_2 = z_3 - z_2, \\ \Delta W_1 + \Delta W_2 = \frac{W}{2}. \end{cases} \quad (6)$$

However, Eq. (5) can be also duplicated in any subsection of the leading edge with given length and width. Therefore, the concept of “fission” at the leading edge is introduced to expand the application scope of Eq. (5). In Fig. 5, three classes of waveriders with  $n=1, 2, 3$ , specifying the number of leading-edge segments, are illustrated. The shape of the waverider at  $n=i$  is referred to as class- $i$  waverider and the class  $i+1$  waverider is the successor of the class  $i$  waverider. The sets of sweep angle distributions  $n=1$  and 2 are defined as  $\kappa = \{A_{11}\}$  and  $\kappa = \{A_{21}, A_{22}\}$ . As in the atomic fission process, the class-2 waverider is derived from the class-1 waverider. Thus, the waverider with a constant sweep (class-1 waverider) angle can derive countless types of waveriders characterized by multi-segment and fixed sweep angles. The “fission” products of the class- $i$  waverider, namely the class- $(i+1)$  waverider, are differentiated according to the leading-edge subsection of the class- $i$  waverider. As shown in Fig. 5, the class-2 waverider only has one type successor of class-1 waverider due to the constant sweep angle as  $\kappa = \{A_{11}\}$ . For the class-2 waverider, the leading-edge used for fission process has two subsections with different sweep angles as  $\kappa = \{A_{21}, A_{22}\}$ . For that, the class-3 waverider will have two types of waverider with the distribution of sweep

angle as  $\kappa = \{A_{31}, A_{32}, A_{33}\}$ . By deduction, there is a relationship between the numbers of adjacent class waveriders ( $k_n$  and  $k_{n-1}$ ), which is depicted as

$$k_n = \frac{k_{n-1} \cdot (2n - k_{n-1} - 1)}{2}, \quad n > 1. \quad (7)$$

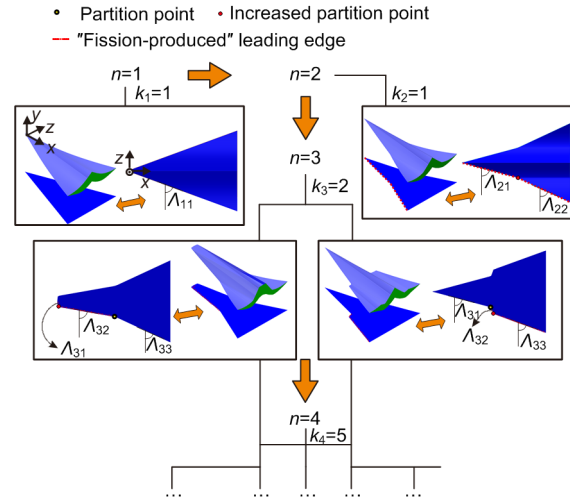


Fig. 5 Waverider fission process

## 2.2.2 Adjustable dihedral angle

The adjustable dihedral angle is controlled by the endpoint of the base-plane lower surface profile curve (Etkin and Reid, 1996), as shown in Figs. 1 and 2. The dihedral angle is introduced to the shock profile curve function (Figs. 2 and 4) as an input parameter in the design process. The detailed design process will be discussed in the section on parametric modelling.

## 2.3 Design examples

Based on the design method presented in the previous section, as shown in Figs. 6 and 7, the geometries of design examples with different sweep angles or dihedral angles are generated. As presented in Fig. 6, two different sweep angle combination schemes are used in different waveriders with given length and width. As Fig. 6 denotes, the two waveriders have the same dihedral angle. Furthermore, the dihedral angle can be adjusted without changing the sweep angle. As depicted in Fig. 7, positive and negative dihedral angles are respectively assigned to two different waveriders. Meanwhile, they have the same planform contour and the same sweep angle distribution along the spanwise direction.

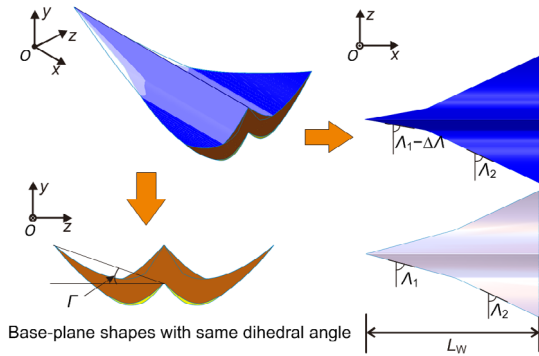


**Fig. 6** Waveriders with different sweep angles ( $\Lambda$ ) and the same dihedral angle ( $\Gamma$ )

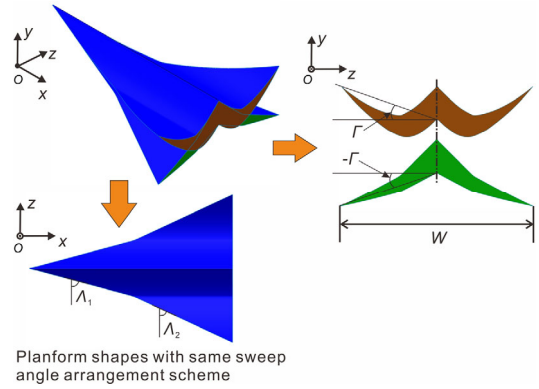


**Fig. 7** Waveriders with different dihedral angles ( $\Gamma$ ) and the same sweep angle ( $\Lambda$ )

Previously in this study, the concept of an osculating cone waverider with adjustable sweep and dihedral angles has been clarified. For research convenience, the LEPC illustrated in Fig. 2 is characterized by two constant sweep angles ( $\Lambda_1$  and  $\Lambda_2$ ), as shown in Fig. 8:

$$\begin{aligned} \min(\tan \Lambda_1, \tan \Lambda_2) &< \tan \Lambda \\ &< \max(\tan \Lambda_1, \tan \Lambda_2). \end{aligned} \quad (8)$$

Note that the two different constant sweep angles ( $\Lambda_1$  and  $\Lambda_2$ ) are restricted by Eq. (8).  $\Lambda$  in Eq. (8) implies the aspect ratio of waverider as expressed in Eq. (9).

$$\tan \Lambda = \frac{L_w}{W/2}. \quad (9)$$

The dihedral angle depends on the position of point  $P_t$  in Fig. 9, which is also closely related to the shock wave profile curve (SPC) as illustrated in Fig. 4. Therefore, the dihedral angle is defined in the SPC function. As expressed in Eq. (10), the SPC function is a subsection curve. The inner portion of SPC is a straight line and the outer portion is a cubic curve:

$$\begin{cases} y = 0, & 0 < |z| \leq L_s, \\ y = A(|z| - L_s)^3, & L_s < |z| \leq W/2. \end{cases} \quad (10)$$

As illustrated in Fig. 9,  $L_s$  is the half length of the inner portion of the SPC.  $W/2$  is the half width of the waverider.  $L_s$  and  $W$  are given in advance.  $A$  is an undetermined coefficient, which is calculated according to Eq. (11).  $h_1$  is the vertical distance between points  $P_t$  and  $O$ .  $h_0$  is the vertical distance between points  $P_0$  and  $O$ .  $H$  is the thickness of the waverider on the symmetric plane as depicted in Figs. 9 and 10. It can be calculated according to the streamline on the symmetric plane shown in Fig. 10. Based on the length of the streamline on symmetric plane which is also the length of waverider and the given conical basic flow field, the calculation process of solving the streamline can be completed.

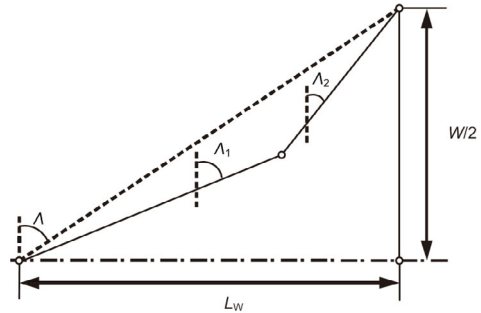


**Fig. 8** Waverider planform geometric characteristics curves (right half)

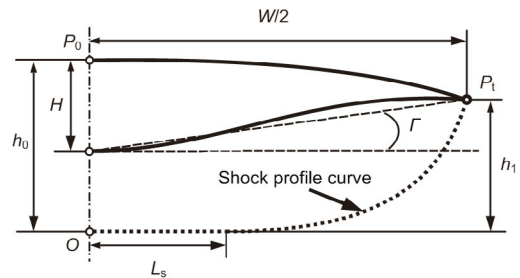


**Fig. 9** Waverider geometric characteristics curves on base plane (right half)



The radius of the corresponding local cone is infinite, which means that the streamline on the symmetric plane is independent of the shock wave curve function. Thus, the undetermined coefficient  $A$  in Eq. (10) can be solved without considering the influence of the parameter  $H$  shown in Fig. 10:

$$A = \frac{h_1}{\left(\frac{W}{2} - L_s\right)^3} = \frac{L_w \tan \beta_s - H + \frac{W}{2} \tan \Gamma}{\left(\frac{W}{2} - L_s\right)^3}. \quad (11)$$

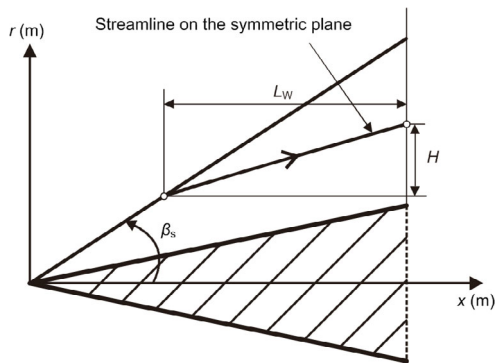


**Fig. 10** Illustration of the streamline on the symmetric plane

$r$  is the cylinder radial axis in the coordinate system

### 3 Case verification

#### 3.1 Case design

In the current study, three waverider cases with adjustable sweep and dihedral angles are generated. The waveriders are designed at  $Ma_\infty=6$ , and  $\beta_s$  as the generating shock wave angle is  $12^\circ$  ( $\beta_s=12^\circ$ ). According to the definition of an osculating cone waverider in Fig. 4, the above input parameters ( $Ma_\infty=6$ ,  $\beta_s=12^\circ$ ) are constant on each osculating plane. The planform shape definition parameters used for geometry design are listed in Table 1.  $L_s$  is set as  $L_s=0.01W$ .

**Table 1** Planform shape parameters of three waverider cases

Case	$L_w$ (m)	$W$ (m)	$A_1$ ( $^\circ$ )	$A_2$ ( $^\circ$ )	$\Gamma$ ( $^\circ$ )
1	6	4.37	75	65	-7
2	6	4.37	80	65	-7
3	6	4.37	75	65	10

The planform and rear view of Cases 1–3 are illustrated in Figs. 11–13, respectively. As shown in Figs. 11a and 11b, the leading-edge sweep angles of Case 1 are  $A_1=75^\circ$  and  $A_2=65^\circ$ , and the dihedral angle ( $\Gamma$ ) of Case 1 is set as  $-7^\circ$  which is also defined as the positive anhedral angle.

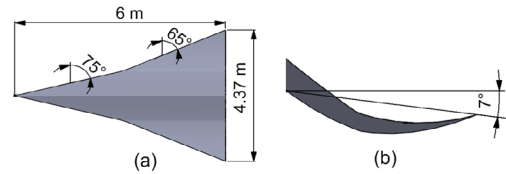


**Fig. 11** Shape views and geometrical parameters of Case 1 (half model)

(a) Planform view; (b) Rear view

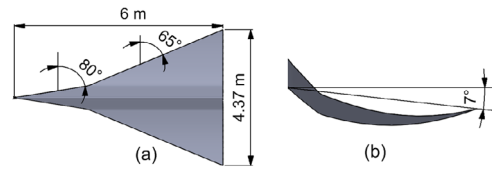


**Fig. 12** Shape views and geometrical parameters of Case 2 (half model)

(a) Planform view; (b) Rear view

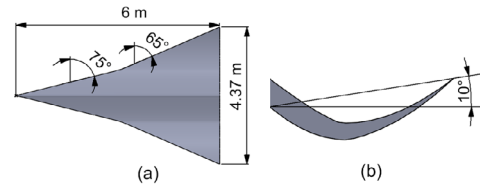


**Fig. 13** Shape views and geometrical parameters of Case 3 (half model)

(a) Planform view; (b) Rear view

#### 3.2 Verification of waverider generation

An unstructured Cartesian mesh Euler code has been employed to numerically simulate the inviscid flow fields and inviscid aerodynamic performance of three waverider cases. The numerical simulations were completed using the reliable commercial software program Cart3D (Rodriguez, 2004; Ding et al., 2015d).

The inviscid dimensionless pressure contours on different  $x$ -coordinate planes of Case 1 under specific design conditions are shown in Figs. 14 and 15.  $P_\infty$  in Figs. 14 and 15 is the static pressure of the freestream

flow. As illustrated in Fig. 14, the predicted shock wave location obtained by the numerical method matches well with the designed shock wave profile curve (Fig. 9) denoted as the dashed curve. As presented in Fig. 15, the high pressure under the waverider on different  $x$ -coordinate planes has almost no leakage to the upper surface. It is obvious that the waverider can ride on the shock wave under the design flight condition and the shock wave will remain attached to the leading-edge across the vehicle. Thus, the design methodology of an osculating cone waverider is validated based on the above discussion.

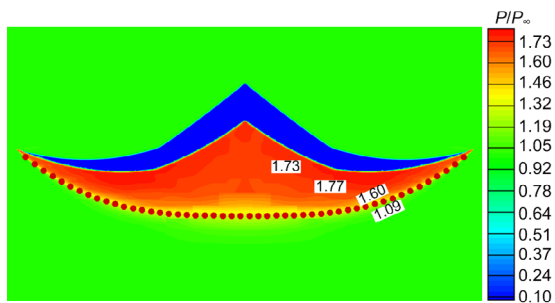


Fig. 14 Dimensionless pressure contour of Case 1 on the base plane

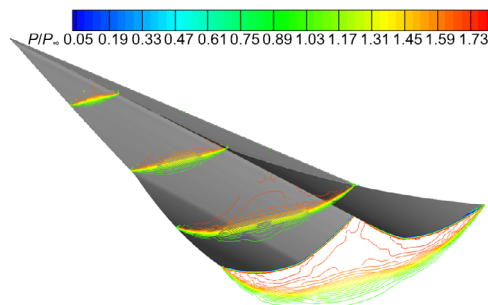


Fig. 15 Dimensionless pressure contour of Case 1 on different  $x$ -coordinate planes

## 4 Performance analysis

The aerodynamic characteristics of the on-design and off-design characteristics of the three waveriders are discussed in the following section, including evaluation of the lift-to-drag ratios and lateral stability.

### 4.1 Lift-to-drag ratio comparison

In this section, the influence of the sweep angles and dihedral angles on the lift-to-drag ratio will be

discussed. Figs. 16–18 show the contrast curves of the lift-to-drag ratio over attack angles of Cases 1–3 at different Mach numbers, respectively. As shown in Figs. 16–18, for supersonic and hypersonic speed stages ( $Ma=2.0$ – $6.0$ ) at the angles of attack ( $\alpha$ ) of  $0^\circ$ – $8^\circ$ , all the verification cases will have a larger lift-to-drag ratio at higher Mach number. The sweep angle and dihedral angle are shown to make no difference to the changing rules of lift-to-drag ratio at different supersonic and hypersonic speed stages.

The sweep angle effect on lift-to-drag ratio seems to focus on the waverider flying at subsonic speed. It is found that the differences in lift-to-drag ratio between low subsonic speeds ( $Ma=0.3$  and  $0.5$ ) and high subsonic speeds ( $Ma=0.8$ ) shown in Fig. 16 are smaller than those shown in Fig. 17. The decrease of  $A_1$  in Case 1 improves  $L/D$  during subsonic speed regime ( $Ma=0.3$  and  $0.5$ ) while keeping  $L/D$  relatively stable at  $Ma=0.8$ . Comparing the results of Figs. 16 and 18, the positive dihedral will further improve the lift-to-drag ratio of the waverider at  $Ma=0.3$ .

To clarify the discussion regarding the effects of sweep angle and dihedral angle on the lift-to-drag ratio of a waverider, the comparison of the maximum lift-to-drag ratios over the Mach numbers of Cases 1–3 is illustrated in Fig. 19. Regarding the maximum lift-to-drag ratio, Case 1 has advantages over other cases at subsonic speeds ( $Ma=0.3$ – $0.8$ ). That is to say, a smaller  $A_1$  improves the lift-to-drag ratio of a waverider in subsonic flight. It is also found that the decrease in  $A_1$  caused little change to the  $L/D$  characteristic at supersonic/hypersonic speed. However, considering the effect of dihedral angle, a distinct decrease of  $L/D$  is observed in Case 3. In terms of maximum lift-to-drag ratios at different Mach numbers shown in Fig. 19, the anhedral angle shown in Fig. 11b is superior to the dihedral angle shown in Fig. 13b. As shown in Tables 2 and 3,  $C_L$  and  $C_D$  are the lift coefficient and drag coefficient of waverider, respectively. By comparing the dihedral effect on the lift and drag coefficients of maximum lift-to-drag ratios shown in Tables 2 and 3, the dihedral effect on drag coefficients can be seen to contribute more to the quantitative difference of maximum lift-to-drag ratio between the dihedral and anhedral angles at supersonic speeds.



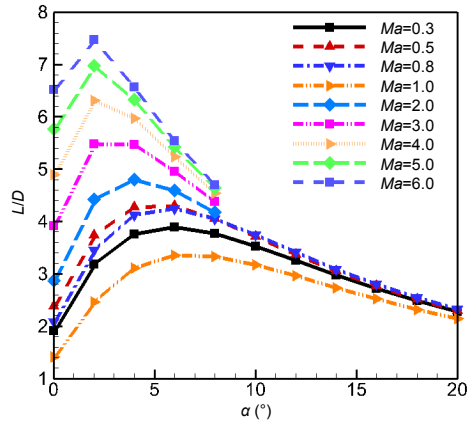


Fig. 16 Curves of lift-to-drag ratio over attack angles of Case 1 at different Mach numbers

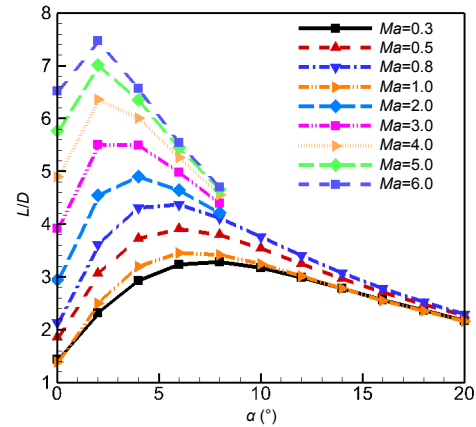


Fig. 17 Curves of lift-to-drag ratio over attack angles of Case 2 at different Mach numbers

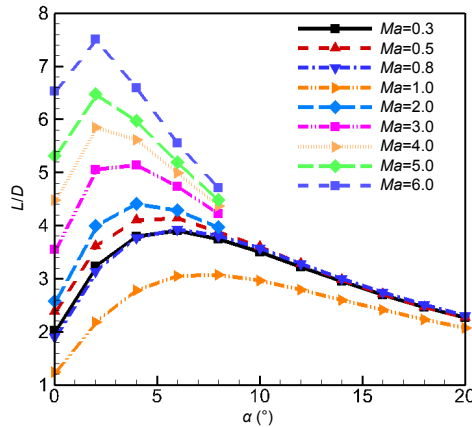


Fig. 18 Curves of lift-to-drag ratio over attack angles of Case 3 at different Mach numbers

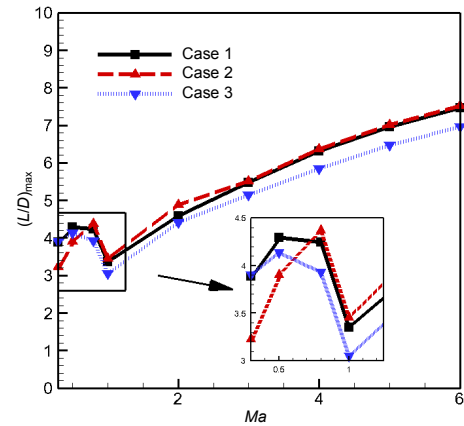


Fig. 19 Curves of maximum lift-to-drag ratio over Mach numbers of Cases 1–3

Table 2 Dihedral effect on lift coefficients of maximum lift-to-drag ratios

$Ma$	$C_L-(L/D)_{\max}$		$\Delta C_L$
	Case 1	Case 3	
4.0	0.0790	0.0791	0.13%
5.0	0.0655	0.0664	1.37%
6.0	0.0565	0.0577	2.12%

Table 3 Dihedral effect on drag coefficients of maximum lift-to-drag ratios

$Ma$	$C_L-(L/D)_{\max}$		$\Delta C_D$
	Case 1	Case 3	
4.0	0.0125	0.0135	8.00%
5.0	0.0094	0.0102	8.51%
6.0	0.0076	0.0083	9.21%

## 4.2 Lateral stability comparison

The lateral stability  $C_{l\beta}$  defined in Eq. (12) is denoted by the derivative of rolling moment coefficients with respect to the angle of sideslip shown in Fig. 20.

$$C_{l\beta} = \frac{\partial C_l}{\partial \beta}. \quad (12)$$

The coefficient  $C_{l\beta}$  is used to evaluate the lateral stability of a waverider. By definition, a vehicle will generate a positive sideslip angle with a positive controlling roll moment ( $C_l$ ). Accordingly, the waverider with negative  $C_{l\beta}$  is laterally stable. In this study, the rolling moment coefficient  $C_l$  of three cases at  $\beta=0^\circ, 2^\circ, 4^\circ$  at different attack angles is computed. The lateral static stability derivative  $C_{l\beta}$  at  $\beta=0^\circ$  is calculated based on the central difference with the

rolling moment coefficient  $C_l$  at  $\beta=2^\circ$  and  $-2^\circ$ . Because of the symmetry of the waverider, the result of  $C_l$  at  $\beta=-2^\circ$  equals the negative value of  $C_l$  at  $\beta=2^\circ$ . The derivative  $C_{l\beta}$  at  $\beta=2^\circ$  is computed by applying the central difference scheme between the rolling moment coefficient  $C_l$  at  $\beta=0^\circ$  and  $4^\circ$ . Similarly, the derivative  $C_{l\beta}$  at  $\beta=3^\circ$  is obtained with the results of  $C_l$  at  $\beta=2^\circ$  and  $4^\circ$ .

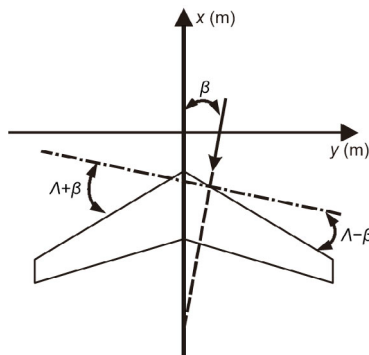


**Fig. 20** Effective sweep angle of left and right wings with sideslip angle  $\beta$

In Figs. 21–23, the comparative curves of  $C_{l\beta}$  (lateral static stability derivative) are shown over attack angles of the three cases at  $Ma=6.0$ . Only Case 3 has laterally static stability at most attack angles ( $\alpha>1^\circ$ ). A large attack angle is seen as better for lateral static stability than a small attack angle. Thus, the dihedral angle is better than the anhedral angle when considering the lateral static stability of a hypersonic waverider. In comparison with the sweep angle, the dihedral angle has a fundamental effect on the lateral static stability of a waverider.

As shown in Fig. 20, the sideslip angle results in a change of the effective sweep angle of the left and right wings. The effective sweep angle of the right wing is  $\Lambda-\beta$  and the effective speed of the leading edge becomes  $V\cos(\Lambda-\beta)$  which is larger than that of the left wing  $V\cos(\Lambda+\beta)$ , where  $V$  is the freestream velocity. Considering the on-design condition with a hypersonic freestream, a larger effective speed will result in a stronger shock wave with a much greater pressure rise after the shock wave. In that case, the lift of the right wing will be slightly larger than that of the left wing due to the pressure rise. Thus, a negative roll moment will be generated at the wings with sweep angle and will be in favor of improving the lateral stability of the whole vehicle. As discussed above, a

larger sweep angle will enlarge the difference of effective speed between the right and left wings. It is also validated by the CFD result of Case 1 and Case 2 shown in Fig. 22 and Fig. 23 that, increasing the forebody sweep angle will improve the lateral static stability of a waverider. However, the waverider with larger forebody sweep angle is still laterally unstable over all the calculated flight attack angles. Thus, the sweep angle has limited influence on the lateral stability compared to the dihedral angle. According to the aerodynamic results of Case 3 and Case 1 shown in Fig. 22 and Fig. 23, the dihedral angle seems to play a central role in the lateral stability of a waverider.

As depicted in Fig. 24, a waverider with dihedral angle will cause a velocity component in the direction normal to the undersurface. The right wing with the positive sideslip angle will have a positive additional effective attack angle ( $\Delta\alpha=\beta\Gamma$ ) while the left wing will have a negative one ( $\Delta\alpha=-\beta\Gamma$ ). The difference of effective attack angle between left and right wings is  $2\beta\Gamma$ . Thus, the right wing will generate a larger lift than the left wing with positive sideslip angle. Furthermore, the unbalanced lift will impose a negative roll moment on the waverider and balance the positive rolling moment bringing about a positive sideslip angle. As illustrated in Figs. 22 and 23, the negative roll moment will be generated only by the waverider with dihedral angle and it helps to convert the waverider's lateral static stability from an unstable state to a stable one. In general, it can be inferred that the negative roll moment generated by an additional effective attack angle is larger than the one generated by changing the effective leading-edge velocity. In the end, the rolling moment of waverider with a sideslip angle will be deeply affected by changing the dihedral angle.

## 5 Conclusions

This study adopts the osculating cone waverider methodology defined by the planform leading edge profile curve and introduces two key design parameters to the waverider design process. The first is the sweep angle of the planform leading-edge profile curve, and the other is the dihedral angle of the underside of the waverider. By controlling the above

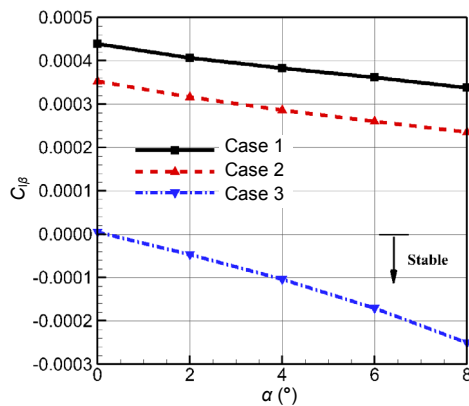


Fig. 21 Curves of lateral stability derivative over attack angles of Cases 1–3 ( $Ma=6.0$ ,  $\beta=0^\circ$ )

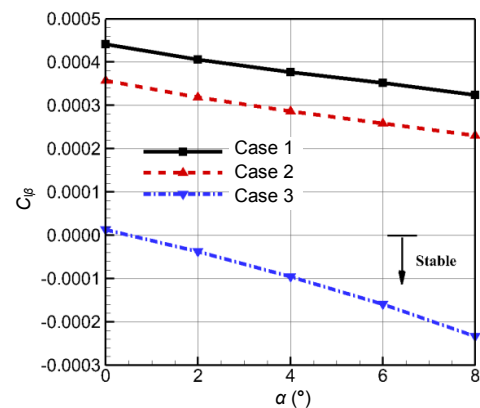


Fig. 22 Curves of lateral stability derivative over attack angles of Cases 1–3 ( $Ma=6.0$ ,  $\beta=2^\circ$ )

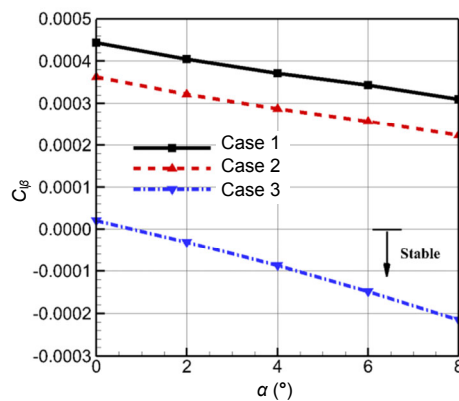


Fig. 23 Curves of lateral stability derivative over attack angles of Cases 1–3 ( $Ma=6.0$ ,  $\beta=3^\circ$ )

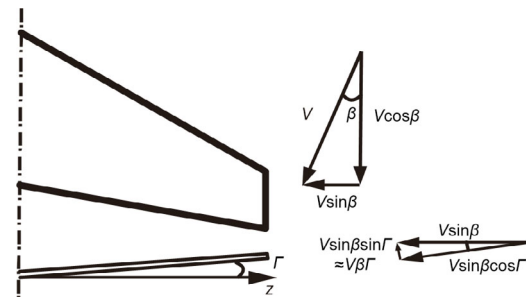


Fig. 24 Effective attack angle change caused by sideslip angle  $\beta$

two parameters, we generate three examples of waveriders with different parameter combination schemes. Through inviscid flow field computation, the waverider design methodology is verified. The effects of sweep and dihedral angles on the lift-to-drag ratio and lateral stability are investigated, and meaningful results are obtained.

Based on these results, we can conclude that, considering the maximum lift-to-drag ratio, the sweep angle plays a role on the lift-to-drag ratio only at subsonic and trans/supersonic speeds as a negligible effect is observed at hypersonic speeds, whereas the dihedral angle is seem to produce a relevant difference at hypersonic speeds. In addition, the effect of sweep angle on maximum lift-to-drag ratio is contradictory at subsonic and trans/supersonic speeds. At the subsonic speed flight stage, the parameter  $A_1$  produces higher efficiency at smaller angles.

For waverider design, the dihedral angle is more

important to the lateral stability of a waverider than the sweep angle. The results show that the dihedral angle is beneficial for lateral stability.

To improve or control the lateral static stability of a waverider, the two key parameters in this study can be adjusted and optimized by various optimization methods. Furthermore, the osculating cone method used in this study is a useful application in the hypersonic design, which requires further improved designs and ideas in the future.

### Contributors

Shao-hua CHEN designed the research, processed the data, and wrote the first draft of the manuscript. Jun LIU and Wei HUANG revised and edited the final version. Feng DING offered the original osculating cone waverider program.

### Conflict of interest

Shao-hua CHEN, Jun LIU, Wei HUANG, and Feng DING declare that they have no conflict of interest.

## References

- Adamczak DW, Bolender MA, 2015. The flight dynamics of the HIFiRE Flight 6 research vehicle. Proceedings of AIAA Atmospheric Flight Mechanics Conference. <https://doi.org/10.2514/6.2015-0528>
- Ding F, Shen CB, Liu J, et al., 2015a. Influence of surface pressure distribution of basic flow field on shape and performance of waverider. *Acta Astronautica*, 108:62-78. <https://doi.org/10.1016/j.actaastro.2014.11.038>
- Ding F, Liu J, Shen CB, et al., 2015b. Novel approach for design of a waverider vehicle generated from axisymmetric supersonic flows past a pointed von Karman ogive. *Aerospace Science and Technology*, 42:297-308. <https://doi.org/10.1016/j.ast.2015.01.025>
- Ding F, Liu J, Shen CB, et al., 2015c. Novel inlet-airframe integration methodology for hypersonic waverider vehicles. *Acta Astronautica*, 111:178-197. <https://doi.org/10.1016/j.actaastro.2015.02.016>
- Ding F, Liu J, Shen CB, et al., 2015d. Simplified osculating cone method for design of a waverider. Proceedings of ASME Turbo Expo 2015: Turbine Technical Conference and Exposition.
- Ding F, Liu J, Shen CB, et al., 2017. An overview of research on waverider design methodology. *Acta Astronautica*, 140:190-205. <https://doi.org/10.1016/j.actaastro.2017.08.027>
- Ding F, Jun L, Shen CB, et al., 2018. An overview of waverider design concept in airframe/inlet integration methodology for air-breathing hypersonic vehicles. *Acta Astronautica*, 152:639-656. <https://doi.org/10.1016/j.actaastro.2018.09.002>
- Etkin B, Reid LD, 1996. Dynamics of Flight: Performance, Stability and Control, 3rd Edition. John Wiley & Sons, New York, the USA, p.81-86.
- Favaloro N, Rispoli A, Vecchione L, et al., 2015. Design analysis of the high-speed experimental flight test vehicle HEXAFLY-international. Proceedings of the 20th AIAA International Space Planes and Hypersonic Systems and Technologies Conference. <https://doi.org/10.2514/6.2015-3607>
- He X, Rasmussen ML, Cox RA, 1993. Waveriders with finlets. Proceedings of the 11th Applied Aerodynamics Conference. <https://doi.org/10.2514/6.1993-3442>
- He XZ, Le JL, Wu YC, 2009. Design of a curved cone derived waverider forebody. Proceedings of the 16th AIAA/DLR/DGLR International Space Planes and Hypersonic Systems and Technologies Conference. <https://doi.org/10.2514/6.2009-7423>
- Hirschel EH, Weiland C, 2009. Selected Aerothermodynamic Design Problems of Hypersonic Flight Vehicles. Springer, Berlin Heidelberg, Germany, p.103.
- Jones JG, Moore KC, Pike J, et al., 1968. A method for designing lifting configurations for high supersonic speeds, using axisymmetric flow fields. *Ingenieur-Archiv*, 37(1): 56-72. <https://doi.org/10.1007/BF00532683>
- Kontogiannis K, Sóbester A, Taylor N, 2015a. On the conceptual design of waverider forebody geometries. Proceedings of the 53rd AIAA Aerospace Sciences Meeting. <https://doi.org/10.2514/6.2015-1009>
- Kontogiannis K, Cerminara A, Taylor NJ, et al., 2015b. Parametric geometry models for hypersonic aircraft components: blunt leading edges. Proceedings of the 20th AIAA International Space Planes and Hypersonic Systems and Technologies Conference. <https://doi.org/10.2514/6.2015-3580>
- Kontogiannis K, Sóbester A, Taylor N, 2017. Efficient parameterization of waverider geometries. *Journal of Aircraft*, 54(3):890-901. <https://doi.org/10.2514/1.C033902>
- Kuchemann D, 1978. The Aerodynamic Design of Aircraft. Pergamon Press, Oxford, the UK, p.448-451.
- Liao L, Yan L, Huang W, et al., 2018. Mode transition process in a typical strut-based scramjet combustor based on a parametric study. *Journal of Zhejiang University-SCIENCE A (Applied Physics & Engineering)*, 19(6): 431-451. <https://doi.org/10.1631/jzus.A1700617>
- Liu CZ, Duan YH, Cai JS, et al., 2014. Applications of multi-block CST method for quasi-waverider design. Proceedings of the 52nd Aerospace Sciences Meeting. <https://doi.org/10.2514/6.2014-0189>
- Liu CZ, Duan YH, Cai JS, et al., 2016. Application of the 3D multi-block CST method to hypersonic aircraft optimization. *Aerospace Science and Technology*, 50:295-303. <https://doi.org/10.1016/j.ast.2015.06.019>
- Liu CZ, Bai P, Chen BY, 2017. Design and property advantages analysis of double swept waverider. *Acta Aeronautica et Astronautica Sinica*, 38(6):120808 (in Chinese). <https://doi.org/10.7527/S1000-6893.2016.0291>
- Liu Z, Liu J, Ding F, et al., 2017a. Effect of thermochemical non-equilibrium on the aerodynamics of an osculating-cone waverider under different angles of attack. *Acta Astronautica*, 139:288-295. <https://doi.org/10.1016/j.actaastro.2017.07.013>
- Liu Z, Liu J, Ding F, et al., 2017b. Novel methodology for wide-ranged multistage morphing waverider based on conical theory. *Acta Astronautica*, 140:362-369. <https://doi.org/10.1016/j.actaastro.2017.09.006>
- Meng YS, Yan L, Huang W, et al., 2019. Structural design and analysis of a composite wing with high aspect ratio. *Journal of Zhejiang University-SCIENCE A (Applied Physics & Engineering)*, 20(10):781-793. <https://doi.org/10.1631/jzus.A1900271>
- Nonweiler TRF, 1959. Aerodynamic problems of manned space vehicles. *The Aeronautical Journal*, 63(585):521-528. <https://doi.org/10.1017/S0368393100071662>
- Pezzella G, Marini M, Cicala M, et al., 2014. Aerodynamic characterization of HEXAFLY scramjet propelled

- hypersonic vehicle. Proceedings of the 32nd AIAA Applied Aerodynamics Conference.  
<https://doi.org/10.2514/6.2014-2844>
- Rasmussen ML, 1997. Effects of anhedral and finlets on lateral stability of hypersonic waveriders. Proceedings of the 35th Aerospace Sciences Meeting and Exhibit.  
<https://doi.org/10.2514/6.1997-191>
- Rodi PE, 2011. Geometrical relationships for osculating cones and osculating flowfield waveriders. Proceedings of the 49th AIAA Aerospace Sciences Meeting Including the New Horizons Forum and Aerospace Exposition.  
<https://doi.org/10.2514/6.2011-1188>
- Rodi PE, 2015. Integration of optimized leading edge geometries onto waverider configurations. Proceedings of the 53rd AIAA Aerospace Sciences Meeting.  
<https://doi.org/10.2514/6.2015-1700>
- Rodriguez DL, 2004. Multidisciplinary optimization of a supersonic inlet using a Cartesian CFD method. Proceedings of the 10th AIAA/ISSMO Multidisciplinary Analysis and Optimization Conference.  
<https://doi.org/10.2514/6.2004-4492>
- Sobieckzy H, Dougherty FC, Jones K, 1990. Hypersonic waverider design from given shock waves. Proceedings of the 1st International Waverider Symposium.
- Strohmeier D, 1998. Lateral stability derivatives for osculating cones waveriders in sub- and transonic flow. Proceedings of the 8th AIAA International Space Planes and Hypersonic Systems and Technologies Conference.  
<https://doi.org/10.2514/6.1998-1618>
- Strohmeier D, Eggers T, Heinze W, et al., 1996. Planform effects on the aerodynamics of waveriders for TSTO missions. Proceedings of Space Plane and Hypersonic Systems and Technology Conference.  
<https://doi.org/10.2514/6.1996-4544>
- Tian C, Li N, Gong GH, et al., 2013. A parameterized geometry design method for inward turning inlet compatible waverider. *Chinese Journal of Aeronautics*, 26(5):1135-1146.  
<https://doi.org/10.1016/j.cja.2013.07.003>
- Viviani A, Pezzella G, 2015. Aerodynamic and Aerothermodynamic Analysis of Space Mission Vehicles. Springer, Switzerland, p.87-91.
- Walker SH, Sherk J, Shell D, et al., 2008. The DARPA/AF falcon program: the hypersonic technology vehicle #2 (HTV-2) flight demonstration phase. Proceedings of the 15th AIAA International Space Planes and Hypersonic Systems and Technologies Conference.  
<https://doi.org/10.2514/6.2008-2539>
- Wang P, Shen CB, 2019. Characteristics of mixing enhancement achieved using a pulsed plasma synthetic jet in a supersonic flow. *Journal of Zhejiang University-SCIENCE A (Applied Physics & Engineering)*, 20(9):701-713.  
<https://doi.org/10.1631/jzus.A1900130>
- Wen X, Liu J, Li J, et al., 2019. Design and numerical simulation of a clamshell-shaped inlet cover for air-breathing hypersonic vehicles. *Journal of Zhejiang University-SCIENCE A (Applied Physics & Engineering)*, 20(5):347-357.  
<https://doi.org/10.1631/jzus.A1800620>
- Wood RM, Bauer SXS, 2001. Flying wings/flying fuselages. Proceedings of the 39th Aerospace Sciences Meeting and Exhibit.  
<https://doi.org/10.2514/6.2001-311>
- Zhang TT, Wang ZG, Huang W, et al., 2019. The overall layout of rocket-based combined-cycle engines: a review. *Journal of Zhejiang University-SCIENCE A (Applied Physics & Engineering)*, 20(3):163-183.  
<https://doi.org/10.1631/jzus.A1800684>
- Zhang WH, Liu J, Ding F, et al., 2019. Novel integration methodology for an inward turning waverider forebody/inlet. *Journal of Zhejiang University-SCIENCE A (Applied Physics & Engineering)*, 20(12):918-926.  
<https://doi.org/10.1631/jzus.A1900334>

## 中文概要

**题目：**后掠角及反角可控的吻切锥乘波体设计方法

**目的：**在飞行器设计中，后掠角及反角会对飞行器的升阻比及横向静稳定性带来影响。本文基于吻切锥乘波体设计方法，将后掠角及反角引入到乘波体的设计过程中，以期实现吻切锥乘波体后掠角及反角的可控设计。

**创新点：**1. 通过理论推导建立后掠角及反角与吻切锥乘波体设计中前缘线在水平面投影型线以及激波底部型线的关系；2. 通过数值计算，研究后掠角及反角研究对吻切锥乘波体升阻比及横向静稳定性的影响。

**方法：**1. 引入基于水平投影型线的吻切锥乘波体设计方法，给出一种前缘点求解方案（图 2 和 4）；2. 通过理论推导，构建设计参数（后掠角与反角）与乘波体设计输入型线的关系（公式（10）和（11））；3. 通过数值模拟，验证设计方法的可行性和有效性（图 14 和 15），以及分析非设计点和设计点下后掠角及反角对乘波体升阻比及横向静稳定性的影响（图 17~19，21~23）。

**结论：**1. 考虑到最大升阻比，后掠角仅在亚音速和跨/超音速时对升阻比起作用，在高超音速时其影响几乎可以忽略；2. 在高超音速时，反角会对升阻比产生影响；3. 对于乘波器的设计，考虑横向静稳定性时，反角比后掠角更重要；4. 下反角有利于横向静稳定性。

**关键词：**吻切锥乘波体；前缘线水平投影型线；后掠角；反角；升阻比；横向静稳定性